### OWT: A Foundational Organ-Wise Tokenization Framework for Medical Imaging

Sifan Song<sup>1\*</sup>, Siyeop Yoon<sup>1\*</sup>, Pengfei Jin<sup>1</sup>, Sekeun Kim<sup>1</sup>, Matthew Tivnan<sup>1</sup>, Yujin Oh<sup>1</sup>, Runqi Meng<sup>1</sup>, Ling Chen<sup>1</sup>, Zhiliang Lyu<sup>1</sup>, Dufan Wu<sup>1</sup>, Ning Guo<sup>1</sup>, Xiang Li<sup>1†</sup>, Quanzheng Li<sup>1†</sup>

Center for Advanced Medical Computing and Analysis (CAMCA),

Massachusetts General Hospital and Harvard Medical School, Boston, USA

### **Abstract**

Recent advances in representation learning often rely on holistic embeddings that entangle multiple semantic components, limiting interpretability and generalization. These issues are especially critical in medical imaging, where downstream tasks depend on anatomically interpretable To address these limitations, we propose an Organ-Wise Tokenization (OWT) framework with a Token Group-based Reconstruction (TGR) training paradigm. Unlike conventional approaches, OWT explicitly disentangles an image into separable token groups, each corresponding to a distinct organ or semantic entity. Our design ensures each token group encapsulates organ-specific information, boosting interpretability, generalization, and efficiency while enabling fine-grained control for targeted clinical applications. Experiments on CT and MRI datasets demonstrate OWT's power: it not only achieves strong performance on standard tasks like image reconstruction and segmentation, but also unlocks novel, high-impact clinical capabilities including organ-specific tumor identification, organ-level retrieval and semantic-level generation, without requiring any additional training. These findings underscore the potential of OWT as a foundational framework for semantically disentangled representation learning, offering broad scalability and a new perspective on how representations can be leveraged.

### 1. Introduction

Representation learning has advanced rapidly in recent years, with growing impact across both natural and medical imaging domains, enabling more effective feature extraction and improved performance across a wide range of

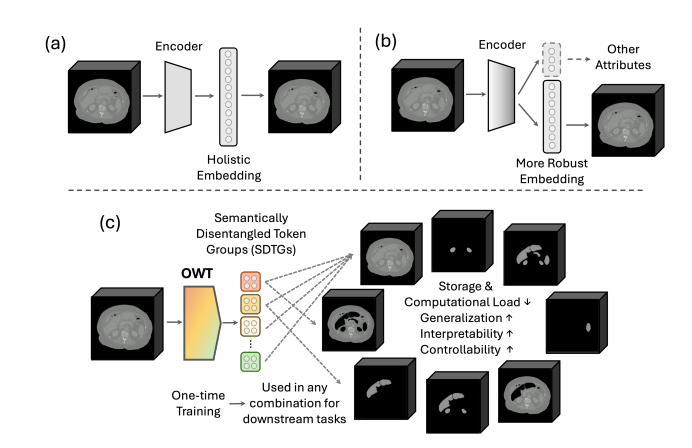


Figure 1. Objective comparison of (a) holistic embedding-based representation learning, (b) disentangled representation learning, and (c) our OWT framework. Unlike prior methods, our foundational tokenization framework enables the extraction of disentangled token groups containing semantically meaningful organ-specific representations. These token groups can be leveraged separately or in combination for downstream analyses, such as semantic-level reconstruction, segmentation, and retrieval.

downstream tasks. Building on this progress, a variety of self-supervised and task-guided training frameworks have been widely adopted, typically relying on holistic embeddings that capture aggregated information for an entire image without explicitly separating semantically distinct components. [22, 55, 59] (Fig.1-a). Similar trends appear in the medical imaging domain, where holistic representations have also been extensively explored for tasks like disease diagnosis [50], organ segmentation [5, 26, 47], and anatomical structure analysis [43, 60]. Although holistic embeddings have shown strong performance, they remain globally mixed within a latent space, entangling information across multiple organs and background regions without explicit semantic separation. This mixed representation poses significant challenges for where fine-grained interpretabil-

<sup>\*</sup>Co-first authors

 $<sup>^{\</sup>dagger}$  Corresponding authors: Contact li.quanzheng@mgh.harvard.edu

ity and a semantically targeted focus are critically important [6, 49, 59].

On the other hand, disentangled representation learning (DRL) aims to decompose data into semantically meaningful factors, each capturing an independent aspect of the underlying variation [59] (Fig.1-b). DRL isolates latent factors (e.g., shape, color, orientation) in natural images [4, 12, 62, 65] or modality attributes in medical images [8, 46], thereby improving explainability and enabling controllable feature manipulation. However, most existing DRL approaches rely on purely data-driven or perturbationdriven strategies, requiring extensive modeling assumptions or specialized regularizers to ensure each factor corresponds to a semantically coherent concept [40, 59]. Consequently, existing DRL approaches suffer from limited alignment with real-world semantics, weak spatial correspondence, and poor scalability (More details on Related Work are provided in Appendix A).

While DRL offers a promising direction, both holistic embeddings and existing disentanglement approaches remain limited in medical imaging scenarios, where organlevel interpretability and analysis are important (e.g., anatomical analysis and surgical planning). These limitations manifest in two key aspects: (a) a lack of interpretability and generalizability, as multiple semantic cues are often entangled without alignment to real-world concepts, making it difficult to isolate relevant structures from confounding factors (e.g., background); and (b) limited efficiency and controllability, as these approaches operate on fused representations rather than isolated organ-level features, restricting the ability to selectively manipulate or analyze distinct semantic factors. These limitations motivate the development of our novel representation learning framework that explicitly tokenizes images at the organ or semantic level.

In this paper, we propose a foundational **Organ-Wise Tokenization (OWT)** framework and a novel **Token Group-based Reconstruction (TGR)** training paradigm (Fig. 1-c). The OWT framework extends a standard encoder-decoder architecture, such as Masked Autoencoders (MAE) or VQGAN, by incorporating two specialized modules: **Organ Collector** and the **Adaptive Holistic Embedding Restorer (AHER)**, which are inspired by prior work on semantic tokenization [17, 18, 48].

The Organ Collector integrates holistic embeddings into semantically meaningful **Token Group** (**TG**), while AHER enables to reconstruct holistic representations from any number of token groups. This design enables a transition pathway from holistic → semantic → holistic embeddings, facilitating both organ-specific processing and reconstruction. To ensure that the extracted semantic embeddings function as true Semantically Disentangled Token Groups (**SDTGs**), the proposed TGR training paradigm explicitly enforces correspondence between each token group and its

target organ. These components constitute a unified framework that encodes organ-specific semantics into modular and reusable TGs, enabling task-adaptive control and restricting computation to relevant semantic regions without additional training, thereby enhancing interpretability and eliminating redundant processing.

We evaluate the organ-wise embeddings on downstream tasks (e.g., image reconstruction and segmentation). Across multiple modalities (CT, two MRI sequences, and a facial dataset), our method consistently outperforms strong baselines, including VAE [33], MAE [28], and state-of-the-art task-specific segmentation architectures such as UNet++ [64], AttU\_Net [44], TransUNet [9], Swin-UNet [5], and CMUNet [52]. Beyond these general tasks, OWT unlocks capabilities that conventional models cannot provide: organ-level tumor identification and retrieval, semantic-level generation, and flexible combination of organ embeddings to adapt to heterogeneous downstream requirements. This demonstrates that the semantic disentanglement enabled by our OWT framework can be leveraged for broader real-world applications, offering a new perspective on how representations can be constructed and utilized.

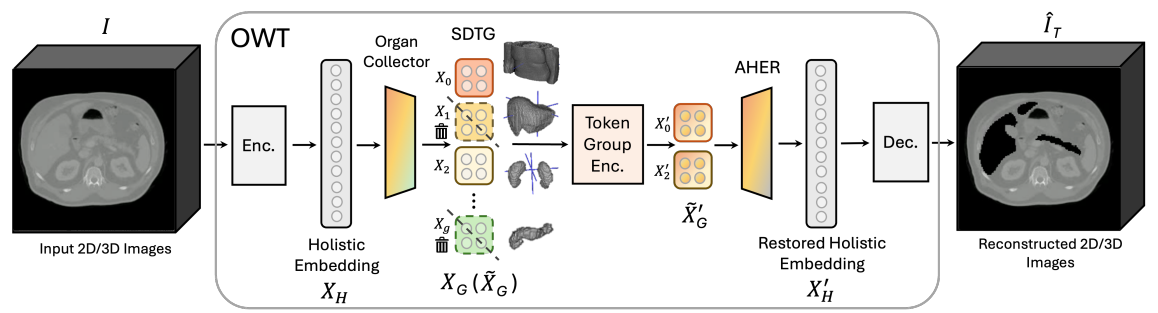
In summary, our contributions are listed as follows:

- We introduce OWT, the first organ-wise foundational framework that, paired with a novel TGR training paradigm, encapsulates organ-specific semantics into semantically disentangled token groups (SDTGs) within a single training process.
- The learned SDTGs are highly condensed yet rich in information for each target organ, enhancing the *inter*pretability and generalizability of the latent embeddings.
- The SDTGs can be selectively combined and reused, yielding improved efficiency and fine-grained controllability. This unlocks unique organ-level downstream tasks, such as organ-specific retrieval and identification, which are highly demanded in the medical imaging domain.
- Our experiments demonstrate significant scalability, as OWT adaptively disentangles semantic information across diverse modalities and domains. This includes a real-world facial dataset, highlighting its potential for applications beyond medical imaging.

### 2. Method

We propose Organ-Wise Tokenization (OWT) with Token Group-based Reconstruction (TGR): OWT encodes each organ into a semantically disentangled token group (SDTG) that can be used alone or composed for downstream tasks.

Overall, the proposed OWT framework comprises five components (Fig. 2): an encoder, Organ Collector, Token Group Encoder, Adaptive Holistic Embedding Restorer (AHER), and a decoder. The encoder maps input images to holistic embeddings, while the Organ Collector and TGR enable the target-organ features to be extracted and stored in



SDTG: Semantically Disentangled Token Group AHER: Adaptive Holistic Embedding Restorer

Figure 2. Overall architecture of Organ-Wise Tokenization (OWT). The input 2D or 3D images are first encoded into holistic embeddings  $(X_H)$ . Then, the holistic tokens are disentangled and embedded in an organ-wise manner using the Organ Collector, forming Semantically Disentangled Token Groups (SDTGs,  $X_G$ ). The SDTGs with solid lines represent randomly retained token groups  $(\tilde{X}_G)$ . The Token Group Encoder further processes these retained groups, capturing both inter- and intra-organ relationships, and transforming them into  $\tilde{X}_G'$ . Finally, an Adaptive Holistic Embedding Restorer and a decoder sequentially restores the holistic representation  $(X_H')$  and reconstructs the final output  $(\hat{I}_T)$ , enabling semantic-level reconstruction.

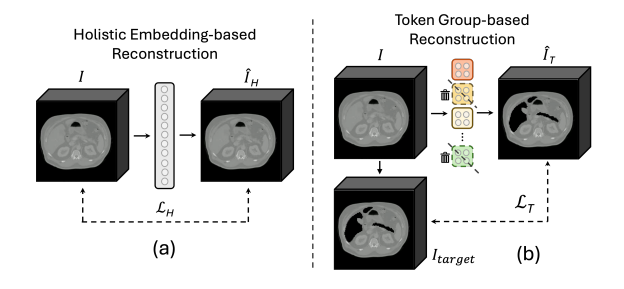


Figure 3. Comparison of the overall process of holistic embedding-based and token group-based reconstruction.

specific embeddings (*i.e.*, SDTGs). In TGR, we randomly select a subset of the predefined token groups. The retained token groups are fed into the Token Group Encoder to integrate both inter-organ and intra-organ information. Next, AHER enables any number of retained token groups to be converted back into a holistic embedding. Finally, the decoder reconstructs an image of the same size as the input.

### 2.1. Encoder and Decoder in OWT

The encoder and decoder in OWT follow standard holistic representation learning architectures, so they can be Transformer-based or (fused) CNN-based, as in 2D/3D MAE [19, 28] or 2D/3D VQGAN [17, 19]. This design choice allows the framework to be applied to either 2D or 3D images with minimal modification. For a 3D input volume processed by a Transformer-based encoder, let  $I \in \mathbb{R}^{D \times H \times W \times C}$ . The encoder (Enc) produces a holistic embedding  $X_H = \mathbf{Enc}(I) \in \mathbb{R}^{(dhw) \times c_e}$ , where D, H, W and C represent the depth, height, width, and channels of the volume, respectively, while d, h and w are the corresponding embedded dimensions. The (dhw) represents the number of tokens processed by the Transformer blocks,

with each token having an embedding dimension of  $c_e$ . This holistic representation is then fed into subsequent modules for more fine-grained organ-wise processing.

### 2.2. Organ Collector

To effectively extract semantically meaningful features from holistic embedding  $X_H$ , the Organ Collector module dynamically assigns importance to different spatial locations or tokens using a token-wise attention matrix  $A_t$ .

Let  $X_H \in \mathbb{R}^{(dhw) \times c_e}$  be reshaped to  $\mathbb{R}^{c_e \times d \times h \times w}$  before being fed into the Organ Collector (Fig. 2). We then employ a token-wise attention mechanism, defined as:

$$A_t = \text{Softmax}(\text{Flatten}(\alpha(X_H))) \in \mathbb{R}^{N_g \times (hw)}, \quad (1)$$

$$X_G = A_t \operatorname{Flatten}(\gamma(X_H))^T \in \mathbb{R}^{N_g \times c_e},$$
 (2)

where  $N_g$  denotes the number of semantic-based tokens, and both  $\alpha$  and  $\gamma$  are linear layers. Concretely,  $\alpha$  projects the  $(c_e \times d)$ -dimensional input to  $N_g$ , then applies Flatten and Softmax to derive a token-wise attention matrix. This attention matrix is multiplied by  $\gamma(X_H)$  (also flattened and transposed) to obtain  $X_G \in \mathbb{R}^{N_g \times c_e}$ . This ensures that each token group captures the most relevant semantic features.

### 2.3. Token Group-based Reconstruction (TGR)

The TGR training paradigm provides direct supervision of semantic disentanglement to token groups. By enforcing accurate organ-wise feature extraction and reconstruction through the token group-level loss  $\mathcal{L}_T$  (Fig. 3-b), TGR preserves both spatial and textural consistency. Consequently, the extracted semantic tokens serve as semantically disentangled token groups (SDTGs). Through TGR, the Organ Collector adaptively extracts organ-specific information into its corresponding SDTG, assigning each token group to a particular organ.

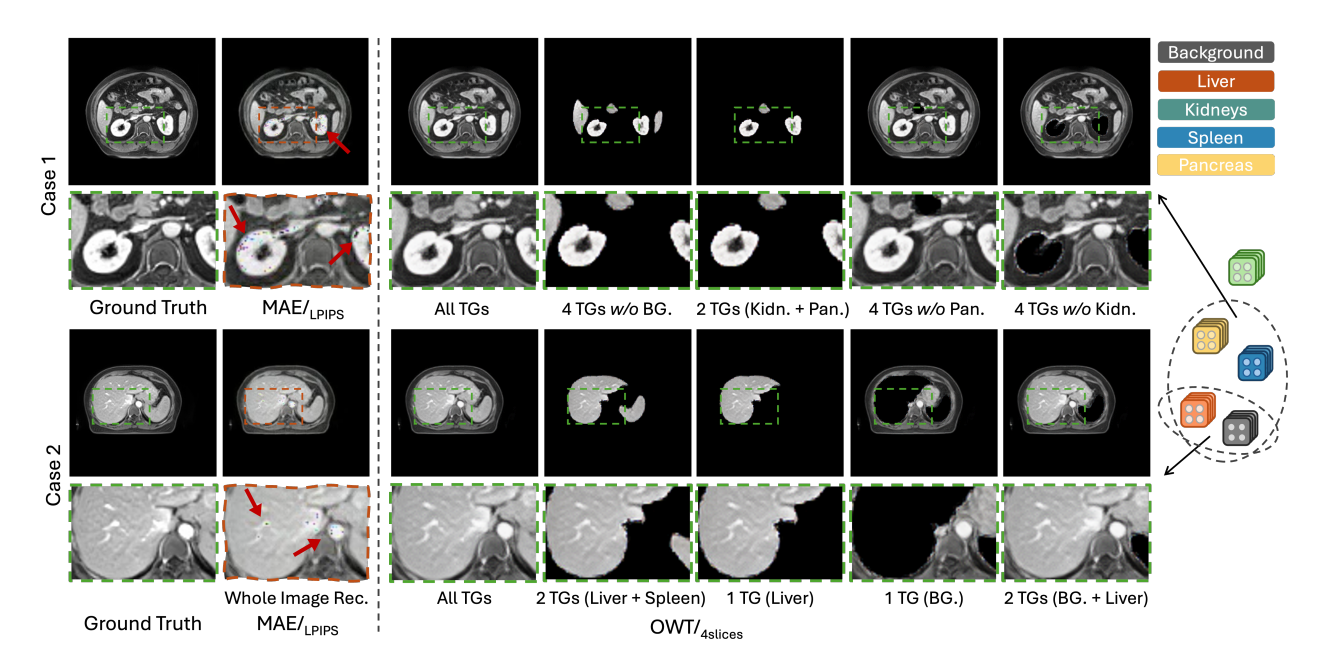


Figure 4. Samples of holistic-based and semantic-based medical image reconstruction from an MRI dataset.

**Definition of Token Group.** Given a dataset D, we have its ground-truth annotations for g semantic group (such as organs in medical image). The remaining regions are treated as background and assigned to a single additional token group. Thus, we define a total of (g+1) token groups. Let each group contain f tokens, making the total number of tokens  $N_g = (g+1) \times f$ . For example, in Fig. 2,  $X_0$ ,  $X_1$ , and  $X_2$  represent the token groups that store liver, kidney, and background information, respectively.

Random Selection Procedure. To establish and preserve the correspondence between token groups and their target organs during training, we apply a two-stage random selection. First, randomly determine the number of retained groups: Let  $\Omega \sim \mathcal{U}(0,1)$  be a uniform random variable on [0,1]. With (g+1) total Token Groups, we define  $\tilde{g} = \lfloor (g+1) \cdot \Omega \rfloor$ , resulting in an integer  $\tilde{g} \in \{0,1,\ldots,g\}$ . Second, randomly select  $\tilde{g}$  groups: From the full set of (g+1) token groups, we then randomly pick exactly  $\tilde{g}$  groups to retain and discard the rest. We set each group to contain f tokens so that each separable and independent token group is in  $\mathbb{R}^{f \times c_e}$ . We concatenate the  $\tilde{g}$  selected groups along the token dimension, producing the final retained token so that  $\tilde{X}_G \in \mathbb{R}^{\tilde{N}_g \times c_e}$  (Fig 2), where the final retained token count is  $\tilde{N}_g = \tilde{g} \times f$ .

During TGR, for each input image, we remain only areas according to randomly retain token groups based on organ annotations (Fig. 3-b), treating the processed image as the target  $I_{target}$  for the token group-based reconstruction loss  $\mathcal{L}_T$ . This explicit supervision encourages a precise organ-level focus, preserving each organ's unique spatial and tex-

tural details in the retained token groups (*i.e.*, SDTGs). Meanwhile, any randomly excluded token groups are discarded at this stage, ensuring that only the retained groups contribute to reconstruction and thereby enhancing semantic flexibility and computational efficiency. As illustrated in Fig. 3, TGR departs from conventional holistic embedding-based reconstruction methods that rely on the latent space for the entire image [2, 17, 19, 28] (Fig. 3-a). By selectively preserving certain token groups, our approach avoids fusing diverse organ features and does not require masked tokens, resulting in improved interpretability, efficiency, and controllability during both reconstruction and subsequent tasks.

After that, we employ a Token Group Encoder  $(\mathbf{Enc}_G)$  composed of six multi-head linear self-attention blocks [32]. Let  $\tilde{X}'_G = \mathbf{Enc}_G(\tilde{X}_G) \in \mathbb{R}^{\tilde{N}_g \times c_e}$  represent the further contextual modeling that captures inter- and intra-organ relationships of the retained token groups.

#### 2.4. Adaptive Holistic Embedding Restorer

Instead of relying on conventional masked tokens, our method discards unselected token groups in the random selection procedure, simplifying training and avoiding unnecessary overhead. After the last module, each input can produce a different number of retained token groups ( $\tilde{X}'_G$  in Fig. 2), resulting in a variable token count  $\tilde{N}_g$ . To convert these tokens back into a representation aligned with the original input size (*i.e.*, the shape of the pre-Organ Collector embedding,  $X_H$ ), we propose an Adaptive Holistic Embedding Restorer (AHER). This module dynamically accepts the variable token count  $\tilde{N}_g$  and restores them to a consis-

Tasks	Organ-specific Identification	Organ-level Retrieval	Pre-defined Rec.	Any Comb. Rec.	Segment- ation
Rec. Nets	Х	×	<b>√</b>	×	Х
Seg. Nets	X	×	×	×	✓
OWT	✓	✓	✓	✓	✓

Table 1. Downstream task capabilities after one-time training.

tent dimension suitable for subsequent reconstruction.

The AHER module is also implemented using a tokenwise attention mechanism, defined as:

$$A_t' = \operatorname{Softmax}(\phi(\tilde{X}_G')^T) \ \in \ \mathbb{R}^{(dhw) \times \tilde{N_g}} \ , \qquad (3)$$

$$X'_{H} = A'_{t} \psi(\tilde{X}'_{G}) \in \mathbb{R}^{(dhw) \times c_{e}}, \qquad (4)$$

where  $\phi(\cdot)$  and  $\psi(\cdot)$  are two linear transformations acting on  $\tilde{X}'_G$ , and (dhw) is the flattened spatial dimension we seek to restore (i.e., the depth  $\times$  height  $\times$  width of the input volume). Specifically, a token-wise attention matrix  $A'_t$  is computed via softmax on the transposed  $\phi(\tilde{X}'_G)$ . Next, the features  $\psi(\tilde{X}'_G)$  are re-aligned according to  $A'_t$ , yielding a restored holistic embedding  $X'_H$  (Fig. 2)

Although  $\tilde{N}_g$  varies per input, this operation preserves organ-specific features while ensuring  $X'_H$  remains a fixed  $(dhw) \times c_e$  shape, thereby maintaining consistency with the decoder. Finally, we pass  $X'_H$  through a standard decoder [28] ( $\mathbf{Dec}$ ) and unpatchify the output, reconstructing the image  $\hat{I}_T = \mathbf{Dec}(X'_H) \in \mathbb{R}^{D \times H \times W \times C}$ .

As mentioned in Sec. 2.3, our objective is to reduce the discrepancy between the target image  $I_{target}$  and the reconstructed image  $\hat{I}_T$ . We combine an L2 term with the LPIPS perceptual loss [63]

$$\mathcal{L}_T = \|I_{target} - \hat{I}_T\|_2^2 + \mathcal{L}_{LPIPS}(I_{target}, \hat{I}_T)$$
 (5)

to preserves low-level fidelity while capturing high-level perceptual similarity, thereby guiding the network to generate more realistic texture and coherent organ regions.

### 3. Datasets and Experimental Setup

We conduct experiments on four 3D medical datasets: two CT sets (Abdomen1k [42] and the CT volumes from AutoPet [21]) and two synthetic MRI sequences (delay and pre-artery) from RAOS dataset [41]. These multimodal and multi-sequence datasets validate the effectiveness and robustness of the OWT framework in medical imaging. To further validate that OWT can generalize to different semantic units beyond medical scenarios, we employ the CelebA-MaskHQ dataset [36]. More details are in *Appendix B.1*, including image preprocessing and data splitting.

All experiments are conducted on six Nvidia H100 GPUs. For fairness, we also add LPIPS loss [63] to VAE and MAE to improve the quality of reconstruction. Further details of the architecture descriptions and hyperparameters are in *Appendix B.2* and *B.3*.

Methods	Enc.	OC.	TG Enc.	AHER	Dec.	Total
MAE	16.66	-	-	- 0.074		27.77
OWT	8.33	0.25	4.25	0.074	11.11	24.01

Table 2. Comparison of computation costs (GFLOPs).

Methods	Disentangled	Used	Tumor Identification	
11104110415	Organ Info.	Token Num.	Liver	Kidneys
MAE	Х	196	73.5	74.7
OWT	✓	20	<b>79.7</b>	81.8

Table 3. Performance for the tumor identification tasks.

### 4. Results

In this section, we design extensive experiments to explore OWT's unique clinical impacts (Sec. 4.2), and to evaluate performance on several downstream tasks (Sec. 4.3). Next, we dive into SDTGs and investigate their semantic characteristics (Sec. 4.4). We also explore the potential of our OWT to address the common issue of limited medical annotations (Sec. 4.5). Finally, we demonstrate that the OWT framework can also be employed in natural image applications (Sec.4.6), and provide ablation studies in *Appendix D* to discuss several important hyperparameters of OWT, including encoder/decoder alterations, different token number per organ, and data percentage used for training.

### 4.1. Advances in Design and Architecture

Due to our proposed TGR training paradigm, the OWT framework produces semantically disentangled token groups (SDTGs) rich in organ-specific information. Leveraging the AHER module, these SDTGs can be individually or flexibly combined and restored from semantic embeddings into their original spatial dimensions. Consequently, as shown in Table 1, OWT requires only one-time training to enable multiple downstream tasks. This crosstask efficiency and controllability significantly distinguish OWT from conventional networks with entangled embeddings, which cannot achieve such flexibility.

OWT is also computationally efficient. As shown in Table 2, OWT requires only 24.01, notably fewer than MAE's 27.77 GFLOPs. This efficiency stems from (1) OWT's semantic tokens containing more highly condensed information than the traditional entangled holistic tokens, and (2) the lightweight design of the Organ Collector (0.25 GFLOPs) and AHER (0.074 GFLOPs) modules.

These designs also offer substantial potential. Specifically, we explore adaptively distributing different token numbers to SDTGs (*e.g.*, based on organ volumes) in *Appendix D.3*. Since Organ Collector and AHER are encoder-decoder independent, we further investigate notable performance gains by replacing Transformer-based structures

Abdomen1k	Н	Holistic Rec.		1 Tok	1 Token Group Rec.		
	L2↓	LPIPS↓	SSIM↑	L2↓	LPIPS↓	SSIM↑	
VAE/ <sub>LPIPS</sub>	6.08e-03	0.1717	-	Х	Х	Х	
MAE	6.74e-04	0.0684	0.9688	Х	X	X	
MAE/LPIPS	6.19e-04	0.0403	0.9722	Х	X	X	
OWT	4.16e-04	0.0390	0.9734	3.31e-04	0.0073	0.9795	
OWT/ <sub>4-slice</sub>	3.69e-04	0.0371	0.9755	2.68e-04	0.0069	0.9838	
	Holistic Rec.						
AutoPet	Н	olistic Rec		1 Tok	en Group l	Rec.	
AutoPet	H	olistic Rec LPIPS↓	SSIM↑	1 Tok	en Group l	Rec. SSIM↑	
AutoPet VAE/LPIPS							
	L2↓	LPIPS↓		L2↓	LPIPS↓	SSIM↑	
VAE/ <sub>LPIPS</sub>	L2↓ 3.43e-03	LPIPS↓ 0.1204	SSIM↑ -	L2↓	LPIPS↓ <b>X</b>	SSIM↑	
VAE/ <sub>LPIPS</sub> MAE	L2↓ 3.43e-03 2.86e-04	LPIPS↓ 0.1204 0.0452	SSIM↑ - 0.9799		LPIPS↓ X X	SSIM↑ X X	

Table 4. Performance of image reconstruction on CT datasets.

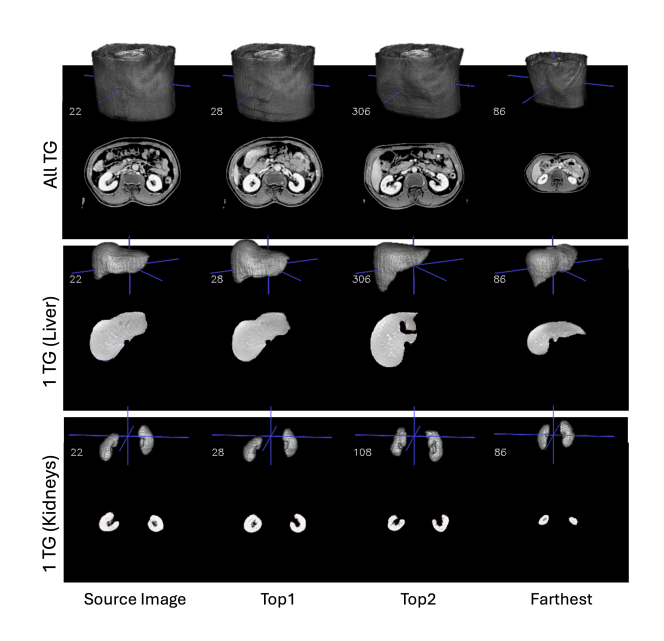


Figure 5. Semantic-based organ-level retrieval of MRI images.

with VQGAN-based alternatives in *Appendix D.1*.

### 4.2. Unique Clinical Impacts

Organ-Specific Tumor Identification. In contrast to conventional models with entangled holistic embeddings, OWT extracts organ-specific information into distinct, semantically disentangled token groups (SDTGs). This structure enables the efficient use of only relevant tokens for highly specific downstream tasks. We demonstrate this on a classification task derived from tumor labels in the Abdomen1k dataset. As shown in Table 3, OWT leverages only 20 organ-specific tokens (*i.e.*, for liver or kidneys) yet achieves significantly better performance than the holistic embedding-based MAE, which utilizes 196 tokens. This results in accuracy improvements of 6.2% (79.7 vs. 73.5) and

Delay	Holistic Rec.			1 Token Group Rec.		
Delay	L2↓	LPIPS↓	SSIM↑	L2↓	LPIPS↓	SSIM↑
VAE/ <sub>LPIPS</sub>	9.88e-03	0.1070	-	Х	Х	Х
MAE	1.37e-03	0.0465	0.9686	X	X	X
MAE/LPIPS	1.36e-03	0.0389	0.9690	X	Х	Х
OWT	7.65e-04	0.0256	0.9851	5.96e-04	0.0088	0.9762
OWT/ <sub>4-slice</sub>	5.81e-04	0.0214	0.9885	5.04e-04	0.0081	0.9801
PreArtery	Н	olistic Rec	-	1 Tok	en Group l	Rec.
PreArtery	H	olistic Rec	SSIM↑	1 Tok	en Group l	Rec. SSIM↑
PreArtery VAE/LPIPS						
	L2↓	LPIPS↓		L2↓	LPIPS↓	SSIM↑
VAE/ <sub>LPIPS</sub>	L2↓ 1.16e-02	LPIPS↓ 0.1059	SSIM↑ -	L2↓	LPIPS↓ <b>X</b>	SSIM↑ <b>X</b>
VAE/ <sub>LPIPS</sub> MAE	L2↓ 1.16e-02 1.67e-03	LPIPS↓ 0.1059 0.0438	SSIM↑ - 0.9701		LPIPS↓  X X	SSIM↑ X X

Table 5. Performance of image reconstruction on MRI datasets.

7.1% (81.8 vs. 74.7) for identifying tumors in the liver and kidneys, respectively, highlighting OWT's ability to create condensed yet highly informative representations for targeted clinical tasks.

Organ-Level Retrieval. Due to their semantic independence, our token groups enable organ-level retrieval ( $L_2$  distance measure), a capability holistic embedding-based models cannot perform (Fig. 5). We demonstrate top-1, top-2, and maximum-distance retrieval results on the MRI modality (CT examples are in Appendix F), where case indices in the top-left corner show results for different organs of interest. Since each token group preserves its organ's spatial structure and texture details, this targeted retrieval is highly beneficial in medical scenarios. For example, it can help radiologists quickly locate similar organ regions across patients without being influenced by other organs, facilitate region-based pathology comparisons, or assist in selecting reference images for organ-specific diagnoses.

### 4.3. Downstream Analysis

**Image Reconstruction.** We evaluate OWT's reconstruction capability on four datasets (two CT, two MRI) [21, 41, 42]. Tables 4 and 5 show OWT outperforms MAE on L2, LPIPS, and 3D SSIM metrics in holistic reconstruction. Moreover, leveraging a 3D kernel for patch embedding in the encoder to tokenize four-slice 3D volumes (OWT/4-slice) generates better results than the 2D OWT variant.

We further explore semantic-based reconstruction by retaining a single organ-wise token group, which is fed through AHER and the decoder to generate an organ-specific image. As reported in Tables 4 and 5, using more slices leads to more robust token groups and improves semantic reconstruction quality. Fig. 4 illustrates this on MRI cases: even with LPIPS added, MAE suffers from noticeable detail loss (red arrows), whereas OWT (all token groups retained) produces sharper, clearer details. Additionally, token groups can be freely combined to reconstruct

1- / 4-slice	C	T	MRI	
- ,	Abdmen1k	AutoPet	Delay	PreArtery
UNetplus	88.38 / 89.78	89.29 / 91.04	84.11 / 85.50	84.42 / 85.68
AttU_Net	89.34 / 90.75	89.73 / 91.46	84.54 / 86.75	85.04 / 86.52
TransUnet	88.91 / 90.24	89.70 / 91.34	84.97 / 86.40	84.29 / 86.01
Swin-Unet	86.56 / 89.47	88.06 / 89.91	83.07 / 85.39	82.41 / 84.48
CMUNet	88.33 / 90.92	89.48 / <b>91.50</b>	84.82 / 86.82	85.56 / 86.94
OWT	89.30 / <b>91.37</b>	89.52 / 91.41	85.85 / <b>87.72</b>	85.67 / <b>87.31</b>

Table 6. Dice performance (1-/4-slice) of semantic segmentation.

AutoPet	Holistic	Holistic Rec.		1 TG Rec.		
114101 01	L2↓	SSIM↑	L2↓	SSIM↑	Dice↑	
MAE/ <sub>LPIPS</sub>	3.58e-04	0.9872	Х	Х	Х	
AttU_Net	Х	X	X	X	87.03	
CMUNet	Х	X	X	X	87.89	
OWT	1.12e-04	0.9909	4.07e-04	0.9765	87.54	
OWT/ <sub>4-slice</sub>	9.34e-05	0.9924	3.60e-04	0.9798	89.42	

Table 7. Generalization capability of cross-dataset experiments trained on Abdomen1k and tested on AutoPet.

only content of interest.

The zoom-in rows of Fig. 4 show that the liver/kidney reconstruction appears nearly identical whether using only its specific token group or combining it with others, suggesting OWT's organ token groups are highly semantically independent. This property enhances interpretability and controllability, enabling reconstruction without unnecessary entanglement of unrelated organ features.

**Image Segmentation.** Reconstructing OWT's token groups preserves clear spatial details and boundaries (Fig. 4). Consequently, a simple thresholding operation on the predictions can generate semantic binary masks, offering direct evidence of each organ-wise token group's independence and interpretability (More details on the thresholding operation are in *Appendix B.3*). Table 6 reports the single-organ segmentation Dice scores (averaged over the liver, kidneys, spleen, and pancreas). For fair comparison, all networks report segmentation results based on 1 and 4 slices. Overall, the accuracy of OWT incorporating information from adjacent slices (OWT with 4-slice) achieves comparable or superior performance across CT and MRI datasets. Detailed per-organ Dice comparisons are in *Appendix E*.

Generalization. Table 7 reports the generalization performance when all methods are trained on Abdomen1k and tested on the AutoPet dataset. Under both reconstruction and segmentation metrics, OWT/4-slice outperforms holistic-based approaches. It also achieves strong results in single-organ reconstruction and segmentation, indicating that to-ken groups can be flexibly combined to mitigate interference from irrelevant organs and background regions, which is what traditional dedicated reconstruction and segmentation networks cannot do, underscoring OTW's potential as

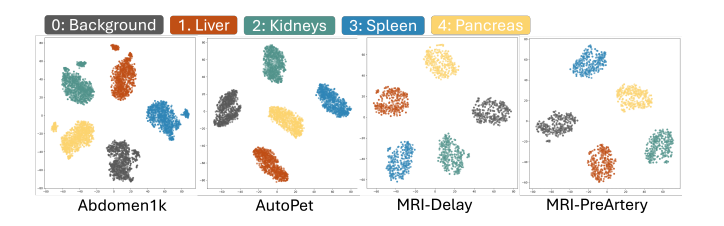


Figure 6. t-SNE visualization of independent token groups on four medical datasets.

AutoPet	Holisti	ic Rec.	1 TG Rec.	
rator et	L2↓	LPIPS ↓	L2↓	LPIPS ↓
OWT	1.49e-04	0.0232	3.32e-04	0.0071
OWT w/ CT-CLIP	1.39e-04	0.0211	3.20e-04	0.0068

Table 8. Reconstruction comparison between OWT w/ and w/o incorporated text prompts.

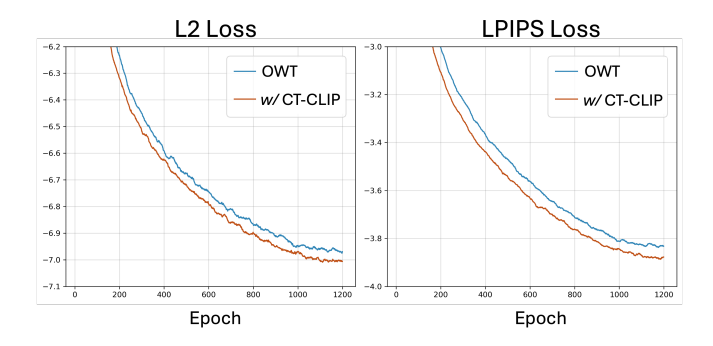


Figure 7. Loss comparison between OWT w/ and w/o incorporated text prompts.

a novel foundational tokenization framework.

#### 4.4. Semantic Information in Token Groups

**T-SNE Analysis.** Fig. 6 illustrates the t-SNE results of how the Organ Collector (with TGR) embeds the background and four organs into the latent space (*i.e.*, five Token Groups) for each dataset. Within this space, token vectors of the same group type exhibit dense clusters, whereas different token groups remain distinctly separated. This clear inter-group separation highlights the semantic independence of organ-specific token groups in OWT.

**Multi-Modality Incorporation.** OWT's highly disentangled and independent SDTGs enable efficient alignment or incorporation with other modalities, such as text. We demonstrate this by encoding medical prompts with a CT-CLIP encoder (specifically pretrained on paired CT images and reports) [25], and adding the resulting organ-specific and CT-consistent text embeddings element-wise to their corresponding token groups. More details on prompts and architecture for training OWT with text encoding are in *Ap*-

AutoPet	Data	Holisti	Holistic Rec.		1 TG Rec.	
ridior ct	Percent	L2↓	LPIPS ↓	L2↓	LPIPS↓	Dice↑
OWT	100%	1.49e-04	0.0232	3.32e-04	0.0071	0.8952
OWT	20%	5.54e-04	0.0658	5.70e-04	0.0115	0.8109
OWT/ <sub>semi</sub>	20%	2.83e-04	0.0394	4.84e-04	0.0102	0.8415
OWT	60%	1.86e-04	0.0270	3.49e-04	0.0076	0.8858
OWT/semi	60%	1.60e-04	0.0243	3.35e-04	0.0072	0.8907

Table 9. Performance comparison of OWT in different training strategies.

CelebAMaskHQ	Holistic Rec.		1 Token Group Rec	
Coloor IIVIIIoIII1Q	L2 ↓	LPIPS ↓	L2 ↓	LPIPS ↓
MAE/ <sub>LPIPS</sub>	2.78e-03	0.1157	Х	Х
OWT	2.50e-03	0.1101	2.83e-03	0.0458

Table 10. Performance of OWT on CelebAMaskHQ dataset.

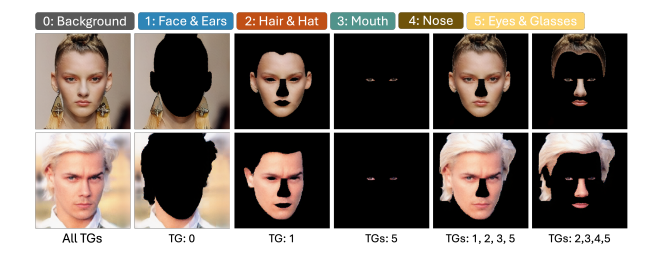


Figure 8. Samples of holistic and semantic-based human face reconstruction on CelebAMaskHQ.

### pendix C.

As shown in Fig. 7 and Table 8, this simple integration accelerates loss convergence and provides immediate improvements in several downstream tasks. This highlights OWT's promise for multi-modal enhancement, unlocking potential applications, such as text-guided retrieval, generation, and improved interpretability in complex workflows.

## 4.5. Semi-Supervised Training under Limited Annotations

The limitation of annotation is a long-standing issue in medical imaging. In our foundational framework, we find that appropriate supervision of token groups is beneficial for downstream tasks. Therefore, we adopted a two-step training strategy: (1) using all data *without* labels for unsupervised pretraining of OWT's encoder and decoder via whole image reconstruction for 600 epochs, and (2) fine-tuning the entire OWT with only *partial* annotation coverage (20% and 60%) from the training set for 1200 epochs.

As shown in Table 9, this approach significantly improves performance under label scarcity. The semi-supervised model using 20% labels greatly outperformed the model trained on only 20% labels. Furthermore, the semi-supervised mode with 60% labels nearly matched the upper-bound results of training with 100% labels, showing

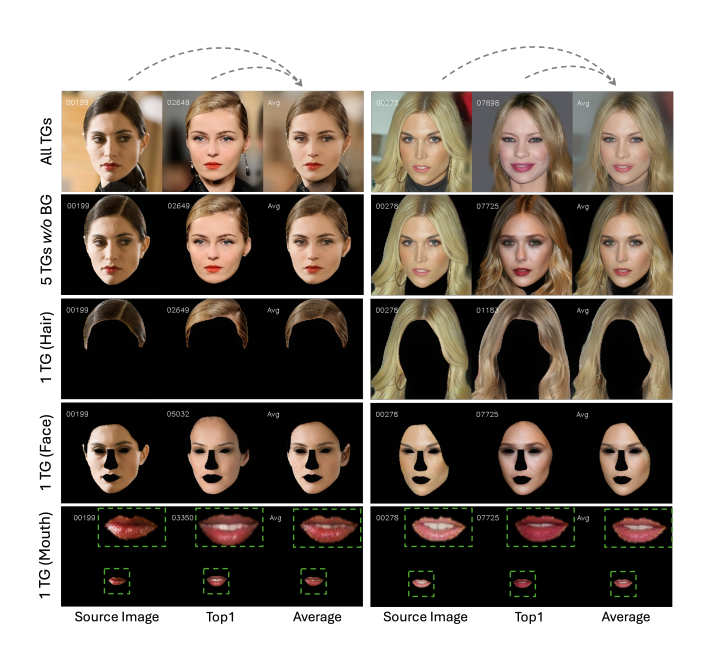


Figure 9. Semantic-based retrieval of CelebAMaskHQ.

OWT's robustness and potential for data-scarce scenarios.

### 4.6. Token Group as Compositional Units

Although OWT and TGR are primarily designed for grouping different semantic components in medical images, they can also be applied to non-medical datasets. As a proof of concept, we demonstrate in Fig. 8 and Table 10 that OWT successfully learns semantically disentangled token groups on the CelebAMaskHQ dataset, capturing and reconstructing each facial region with high spatial and textural fidelity.

As illustrated in Fig. 9, each token group facilitates semantic-based retrieval for different facial attributes (*e.g.*, hair, skin, lips). In the third column, we conduct an experiment by averaging source token group(s) with the Top1 retrieved token group(s). Notably, this averaged token group(s) can still be reconstructed, exhibiting features that blend and transition between both identities (*e.g.*, overall facial attributes, hair color, skin tone, lip color, mouth openness). These observations imply that token groups extracted by OWT can enable fine-grained editing or hybrid generation of facial attributes without background influence, offering enhanced interpretability, efficiency, and controllability.

### 5. Conclusion

In this paper, we propose a novel Organ-Wise Tokenization (OWT) framework and Token Group-Based Reconstruction (TGR) paradigm, which disentangle holistic embeddings into semantically disentangled token groups. Our approach not only improves interpretability, generalizability, efficiency and controllability in organ-based analyses, but also shows adaptability to broader scenarios, including natural image domains. By enabling semantic-level token groups,

OWT enriches unique clinical applications and downstream tasks such as organ-specific analysis, semantic-based reconstruction, segmentation and retrieval, offering a new perspective on how representations can be utilized.

### References

- [1] Gairui Bai, Wei Xi, Xiaopeng Hong, Xinhui Liu, Yang Yue, and Songwen Zhao. Robust and rotation-equivariant contrastive learning. *IEEE Transactions on Neural Networks and Learning Systems*, 2023. 1
- [2] Dor Bank, Noam Koenigstein, and Raja Giryes. Autoencoders. Machine learning for data science handbook: data mining and knowledge discovery handbook, pages 353–374, 2023. 4
- [3] Hangbo Bao, Li Dong, Songhao Piao, and Furu Wei. Beit: Bert pre-training of image transformers. *arXiv preprint arXiv:2106.08254*, 2021. 1
- [4] Christopher P Burgess, Irina Higgins, Arka Pal, Loic Matthey, Nick Watters, Guillaume Desjardins, and Alexander Lerchner. Understanding disentangling in beta-vae. arXiv preprint arXiv:1804.03599, 2018. 2, 1
- [5] Hu Cao, Yueyue Wang, Joy Chen, Dongsheng Jiang, Xi-aopeng Zhang, Qi Tian, and Manning Wang. Swin-unet: Unet-like pure transformer for medical image segmentation. In *European conference on computer vision*, pages 205–218. Springer, 2022. 1, 2
- [6] Irem Cetin, Maialen Stephens, Oscar Camara, and Miguel A González Ballester. Attri-vae: Attribute-based interpretable representations of medical images with variational autoencoders. Computerized Medical Imaging and Graphics, 104:102158, 2023. 2, 1
- [7] Krishna Chaitanya, Ertunc Erdil, Neerav Karani, and Ender Konukoglu. Contrastive learning of global and local features for medical image segmentation with limited annotations. *Advances in neural information processing systems*, 33:12546–12558, 2020. 1
- [8] Agisilaos Chartsias, Thomas Joyce, Giorgos Papanastasiou, Scott Semple, Michelle Williams, David E Newby, Rohan Dharmakumar, and Sotirios A Tsaftaris. Disentangled representation learning in cardiac image analysis. *Medical image* analysis, 58:101535, 2019. 2, 1
- [9] Jieneng Chen, Yongyi Lu, Qihang Yu, Xiangde Luo, Ehsan Adeli, Yan Wang, Le Lu, Alan L Yuille, and Yuyin Zhou. Transunet: Transformers make strong encoders for medical image segmentation. *arXiv preprint arXiv:2102.04306*, 2021. 2, 1
- [10] Ting Chen, Simon Kornblith, Mohammad Norouzi, and Geoffrey Hinton. A simple framework for contrastive learning of visual representations. In *International conference on machine learning*, pages 1597–1607. PmLR, 2020. 1
- [11] Xinlei Chen and Kaiming He. Exploring simple siamese representation learning. In *Proceedings of the IEEE/CVF conference on computer vision and pattern recognition*, pages 15750–15758, 2021. 1
- [12] Xi Chen, Yan Duan, Rein Houthooft, John Schulman, Ilya Sutskever, and Pieter Abbeel. Infogan: Interpretable rep-

- resentation learning by information maximizing generative adversarial nets. *Advances in neural information processing systems*, 29, 2016. 2, 1
- [13] Xiaocong Chen, Lina Yao, Tao Zhou, Jinming Dong, and Yu Zhang. Momentum contrastive learning for few-shot covid-19 diagnosis from chest ct images. *Pattern recognition*, 113: 107826, 2021.
- [14] Rumen Dangovski, Li Jing, Charlotte Loh, Seungwook Han, Akash Srivastava, Brian Cheung, Pulkit Agrawal, and Marin Soljačić. Equivariant contrastive learning. arXiv preprint arXiv:2111.00899, 2021. 1
- [15] Alexandre Devillers and Mathieu Lefort. Equimod: An equivariance module to improve visual instance discrimination. In *International Conference on Learning Representa*tions, 2023. 1
- [16] Alexey Dosovitskiy, Lucas Beyer, Alexander Kolesnikov, Dirk Weissenborn, Xiaohua Zhai, Thomas Unterthiner, Mostafa Dehghani, Matthias Minderer, Georg Heigold, Sylvain Gelly, et al. An image is worth 16x16 words: Transformers for image recognition at scale. arXiv preprint arXiv:2010.11929, 2020. 1
- [17] Patrick Esser, Robin Rombach, and Bjorn Ommer. Taming transformers for high-resolution image synthesis. In *Proceedings of the IEEE/CVF conference on computer vision and pattern recognition*, pages 12873–12883, 2021. 2, 3, 4
- [18] Mohsen Fayyaz, Soroush Abbasi Koohpayegani, Farnoush Rezaei Jafari, Sunando Sengupta, Hamid Reza Vaezi Joze, Eric Sommerlade, Hamed Pirsiavash, and Jürgen Gall. Adaptive token sampling for efficient vision transformers. In *European Conference on Computer Vision*, pages 396–414. Springer, 2022. 2
- [19] Christoph Feichtenhofer, Yanghao Li, Kaiming He, et al. Masked autoencoders as spatiotemporal learners. Advances in neural information processing systems, 35:35946–35958, 2022. 3, 4
- [20] Quentin Garrido, Laurent Najman, and Yann Lecun. Selfsupervised learning of split invariant equivariant representations. arXiv preprint arXiv:2302.10283, 2023. 1
- [21] S. Gatidis and T. Kuestner. A whole-body fdg-pet/ct dataset with manually annotated tumor lesions (fdg-pet-ct-lesions). Dataset, 2022. 5, 6, 1
- [22] Robert Geirhos, Jörn-Henrik Jacobsen, Claudio Michaelis, Richard Zemel, Wieland Brendel, Matthias Bethge, and Felix A Wichmann. Shortcut learning in deep neural networks. *Nature Machine Intelligence*, 2(11):665–673, 2020.
- [23] Spyros Gidaris, Praveer Singh, and Nikos Komodakis. Unsupervised representation learning by predicting image rotations. arXiv preprint arXiv:1803.07728, 2018. 1
- [24] Jean-Bastien Grill, Florian Strub, Florent Altché, Corentin Tallec, Pierre Richemond, Elena Buchatskaya, Carl Doersch, Bernardo Avila Pires, Zhaohan Guo, Mohammad Gheshlaghi Azar, et al. Bootstrap your own latent-a new approach to self-supervised learning. Advances in neural information processing systems, 33:21271–21284, 2020. 1
- [25] Ibrahim Ethem Hamamci, Sezgin Er, Chenyu Wang, Furkan Almas, Ayse Gulnihan Simsek, Sevval Nil Esirgun, Irem Doga, Omer Faruk Durugol, Weicheng Dai, Murong Xu,

- et al. Developing generalist foundation models from a multimodal dataset for 3d computed tomography. *arXiv preprint arXiv:2403.17834*, 2024. 7, 2
- [26] Ali Hatamizadeh, Vishwesh Nath, Yucheng Tang, Dong Yang, Holger R Roth, and Daguang Xu. Swin unetr: Swin transformers for semantic segmentation of brain tumors in mri images. In *International MICCAI brainlesion workshop*, pages 272–284. Springer, 2021. 1
- [27] Kaiming He, Xiangyu Zhang, Shaoqing Ren, and Jian Sun. Deep residual learning for image recognition. In *Proceedings of the IEEE conference on computer vision and pattern recognition*, pages 770–778, 2016. 1
- [28] Kaiming He, Xinlei Chen, Saining Xie, Yanghao Li, Piotr Dollár, and Ross Girshick. Masked autoencoders are scalable vision learners. In *Proceedings of the IEEE/CVF conference on computer vision and pattern recognition*, pages 16000–16009, 2022. 2, 3, 4, 5, 1
- [29] Anjun Hu, Jean-Pierre R Falet, Brennan S Nichyporuk, Changjian Shui, Douglas L Arnold, Sotirios A Tsaftaris, and Tal Arbel. Clinically plausible pathology-anatomy disentanglement in patient brain mri with structured variational priors. arXiv preprint arXiv:2211.07820, 2022. 1
- [30] Gao Huang, Zhuang Liu, Laurens Van Der Maaten, and Kilian Q Weinberger. Densely connected convolutional networks. In *Proceedings of the IEEE conference on computer vision and pattern recognition*, pages 4700–4708, 2017. 1
- [31] Kaida Jiang, Li Quan, and Tao Gong. Disentangled representation and cross-modality image translation based unsupervised domain adaptation method for abdominal organ segmentation. *International Journal of Computer Assisted Radiology and Surgery*, 17(6):1101–1113, 2022. 1
- [32] Angelos Katharopoulos, Apoorv Vyas, Nikolaos Pappas, and François Fleuret. Transformers are rnns: Fast autoregressive transformers with linear attention. In *International conference on machine learning*, pages 5156–5165. PMLR, 2020. 4, 2
- [33] Diederik P Kingma, Max Welling, et al. Auto-encoding variational bayes, 2013.
- [34] Haoran Lai, Zihang Jiang, Qingsong Yao, Rongsheng Wang, Zhiyang He, Xiaodong Tao, Wei Wei, Weifu Lv, and S Kevin Zhou. E3d-gpt: Enhanced 3d visual foundation for medical vision-language model. arXiv preprint arXiv:2410.14200, 2024. 1
- [35] Daniel M Lang, Eli Schwartz, Cosmin I Bercea, Raja Giryes, and Julia A Schnabel. 3d masked autoencoders with application to anomaly detection in non-contrast enhanced breast mri. arXiv preprint arXiv:2303.05861, 2023. 1
- [36] Cheng-Han Lee, Ziwei Liu, Lingyun Wu, and Ping Luo. Maskgan: Towards diverse and interactive facial image manipulation. In *Proceedings of the IEEE/CVF conference on computer vision and pattern recognition*, pages 5549–5558, 2020. 5, 1
- [37] Jie Liu, Yixiao Zhang, Jie-Neng Chen, Junfei Xiao, Yongyi Lu, Bennett A Landman, Yixuan Yuan, Alan Yuille, Yucheng Tang, and Zongwei Zhou. Clip-driven universal model for organ segmentation and tumor detection. In *Proceedings of the IEEE/CVF international conference on computer vision*, pages 21152–21164, 2023. 2

- [38] Tianling Liu, Wennan Liu, Lequan Yu, Liang Wan, Tong Han, and Lei Zhu. Joint prediction of meningioma grade and brain invasion via task-aware contrastive learning. In International Conference on Medical Image Computing and Computer-Assisted Intervention, pages 355–365. Springer, 2022. 1
- [39] Xiao Liu, Pedro Sanchez, Spyridon Thermos, Alison Q O'Neil, and Sotirios A Tsaftaris. Learning disentangled representations in the imaging domain. *Medical Image Analysis*, 80:102516, 2022.
- [40] Francesco Locatello, Stefan Bauer, Mario Lucic, Gunnar Raetsch, Sylvain Gelly, Bernhard Schölkopf, and Olivier Bachem. Challenging common assumptions in the unsupervised learning of disentangled representations. In international conference on machine learning, pages 4114–4124. PMLR, 2019. 2, 1
- [41] Xiangde Luo, Zihan Li, Shaoting Zhang, Wenjun Liao, and Guotai Wang. Rethinking abdominal organ segmentation (raos) in the clinical scenario: A robustness evaluation benchmark with challenging cases. In *International Conference on Medical Image Computing and Computer-Assisted Intervention*, pages 531–541. Springer, 2024. 5, 6, 1
- [42] Jun Ma, Yao Zhang, Song Gu, Cheng Zhu, Cheng Ge, Yichi Zhang, Xingle An, Congcong Wang, Qiyuan Wang, Xin Liu, et al. Abdomenct-1k: Is abdominal organ segmentation a solved problem? *IEEE Transactions on Pattern Analysis and Machine Intelligence*, 44(10):6695–6714, 2021. 5, 6, 1
- [43] MHD Jafar Mortada, Selene Tomassini, Haidar Anbar, Micaela Morettini, Laura Burattini, and Agnese Sbrollini. Segmentation of anatomical structures of the left heart from echocardiographic images using deep learning. *Diagnostics*, 13(10):1683, 2023.
- [44] Ozan Oktay, Jo Schlemper, Loic Le Folgoc, Matthew Lee, Mattias Heinrich, Kazunari Misawa, Kensaku Mori, Steven McDonagh, Nils Y Hammerla, Bernhard Kainz, et al. Attention u-net: Learning where to look for the pancreas. arXiv preprint arXiv:1804.03999, 2018. 2
- [45] Aaron van den Oord, Yazhe Li, and Oriol Vinyals. Representation learning with contrastive predictive coding. arXiv preprint arXiv:1807.03748, 2018. 1
- [46] Jiahong Ouyang, Ehsan Adeli, Kilian M Pohl, Qingyu Zhao, and Greg Zaharchuk. Representation disentanglement for multi-modal brain mri analysis. In *Information Processing in Medical Imaging: 27th International Conference, IPMI 2021, Virtual Event, June 28–June 30, 2021, Proceedings 27*, pages 321–333. Springer, 2021. 2, 1
- [47] Olaf Ronneberger, Philipp Fischer, and Thomas Brox. Unet: Convolutional networks for biomedical image segmentation. In Medical image computing and computer-assisted intervention–MICCAI 2015: 18th international conference, Munich, Germany, October 5-9, 2015, proceedings, part III 18, pages 234–241. Springer, 2015. 1
- [48] Michael S Ryoo, AJ Piergiovanni, Anurag Arnab, Mostafa Dehghani, and Anelia Angelova. Tokenlearner: What can 8 learned tokens do for images and videos? arXiv preprint arXiv:2106.11297, 2021. 2
- [49] Kathryn Schutte, Olivier Moindrot, Paul Hérent, Jean-Baptiste Schiratti, and Simon Jégou. Using stylegan for vi-

- sual interpretability of deep learning models on medical images. arXiv preprint arXiv:2101.07563, 2021. 2, 1
- [50] Dinggang Shen, Guorong Wu, and Heung-Il Suk. Deep learning in medical image analysis. Annual review of biomedical engineering, 19(1):221–248, 2017. 1
- [51] Sifan Song, Jinfeng Wang, Qiaochu Zhao, Xiang Li, Dufan Wu, Angelos Stefanidis, Jionglong Su, S Kevin Zhou, and Quanzheng Li. Contrastive learning via equivariant representation. arXiv preprint arXiv:2406.00262, 2024. 1
- [52] Fenghe Tang, Lingtao Wang, Chunping Ning, Min Xian, and Jianrui Ding. Cmu-net: a strong convmixer-based medical ultrasound image segmentation network. In 2023 IEEE 20th international symposium on biomedical imaging (ISBI), pages 1–5. IEEE, 2023. 2
- [53] Ekin Tiu, Ellie Talius, Pujan Patel, Curtis P Langlotz, Andrew Y Ng, and Pranav Rajpurkar. Expert-level detection of pathologies from unannotated chest x-ray images via self-supervised learning. *Nature biomedical engineering*, 6(12): 1399–1406, 2022. 1
- [54] Ashish Vaswani, Noam Shazeer, Niki Parmar, Jakob Uszkoreit, Llion Jones, Aidan N Gomez, Łukasz Kaiser, and Illia Polosukhin. Attention is all you need. Advances in neural information processing systems, 30, 2017. 2
- [55] Athanasios Voulodimos, Nikolaos Doulamis, Anastasios Doulamis, and Eftychios Protopapadakis. Deep learning for computer vision: A brief review. *Computational intelligence* and neuroscience, 2018(1):7068349, 2018. 1
- [56] Jie Wang, Chaoliang Zhong, Cheng Feng, Ying Zhang, Jun Sun, and Yasuto Yokota. Disentangled representation for cross-domain medical image segmentation. *IEEE Transactions on Instrumentation and Measurement*, 72:1–15, 2022.
- [57] Jinfeng Wang, Sifan Song, Jionglong Su, and S Kevin Zhou. Distortion-disentangled contrastive learning. In Proceedings of the IEEE/CVF Winter Conference on Applications of Computer Vision, pages 75–85, 2024. 1
- [58] Shuai Wang and Rui Li. Semantic-guided disentangled representation for unsupervised cross-modality medical image segmentation. *arXiv preprint arXiv:2203.14025*, 2022. 1
- [59] Xin Wang, Hong Chen, Zihao Wu, Wenwu Zhu, et al. Disentangled representation learning. IEEE Transactions on Pattern Analysis and Machine Intelligence, 2024. 1, 2
- [60] Alexander D Weston, Panagiotis Korfiatis, Timothy L Kline, Kenneth A Philbrick, Petro Kostandy, Tomas Sakinis, Motokazu Sugimoto, Naoki Takahashi, and Bradley J Erickson. Automated abdominal segmentation of ct scans for body composition analysis using deep learning. *Radiology*, 290 (3):669–679, 2019. 1
- [61] Junfei Xiao, Yutong Bai, Alan Yuille, and Zongwei Zhou. Delving into masked autoencoders for multi-label thorax disease classification. In *Proceedings of the IEEE/CVF Winter Conference on Applications of Computer Vision*, pages 3588–3600, 2023. 1
- [62] Taihong Xiao, Jiapeng Hong, and Jinwen Ma. Dna-gan: Learning disentangled representations from multi-attribute images. *arXiv preprint arXiv:1711.05415*, 2017. 2, 1
- [63] Richard Zhang, Phillip Isola, Alexei A Efros, Eli Shechtman, and Oliver Wang. The unreasonable effectiveness of

- deep features as a perceptual metric. In *Proceedings of the IEEE conference on computer vision and pattern recognition*, pages 586–595, 2018. 5
- [64] Zongwei Zhou, Md Mahfuzur Rahman Siddiquee, Nima Tajbakhsh, and Jianming Liang. Unet++: A nested u-net architecture for medical image segmentation. In *Deep learning* in medical image analysis and multimodal learning for clinical decision support: 4th international workshop, DLMIA 2018, and 8th international workshop, ML-CDS 2018, held in conjunction with MICCAI 2018, Granada, Spain, September 20, 2018, proceedings 4, pages 3–11. Springer, 2018. 2,
- [65] Jun-Yan Zhu, Zhoutong Zhang, Chengkai Zhang, Jiajun Wu, Antonio Torralba, Josh Tenenbaum, and Bill Freeman. Visual object networks: Image generation with disentangled 3d representations. Advances in neural information processing systems, 31, 2018. 2, 1

### OWT: A Foundational Organ-Wise Tokenization Framework for Medical Imaging

### Supplementary Material

### A. Related Work

## **A.1.** Holistic Embedding-based Representation Learning

Holistic embedding-based approaches map entire 2D/3D inputs into a single latent representation, aiming to capture global image features [22, 55, 59]. These methods typically follow either self-supervised or task-guided strategies. In self-supervised learning, contrastive techniques like Sim-CLR [10], SimSiam [11], and BYOL [24] enforce consistency between augmented views, while predictive approaches such as CPC [45] and RotNet [23] reconstruct missing or permuted portions. Recently, masked image modeling (e.g., MAE [28] and BEiT [3]) has emerged as an effective approach by requiring models to infer masked regions. Meanwhile, task-guided frameworks focus on extracting features that directly benefit a target task, typically resulting in holistic embeddings. Many classic neural networks, such as ResNet [27], DenseNet [30], and Vision Transformer [16], and their variants incorporate classification, regression, or segmentation objectives.

In medical imaging, holistic representations have been widely used for self-supervised feature learning in CT [13, 34], MRI [7, 35], and X-ray [53, 61]. Additionally, classical supervised pipelines (*e.g.*, U-Net [47] and its variants [5, 9, 26, 64]) rely on a global bottleneck to embed entire images or volumes, demonstrating strong performance in organ segmentation and disease detection. Although such approaches achieve notable success, they often encode multiple semantic factors, such as multiple organs and the surrounding background, into an entangled representation with limited interpretability and fine-grained control [6, 49, 59].

### A.2. Disentangled Representation Learning

In contrast to holistic embedding-based approaches, various disentangled representation learning (DRL) studies have pursued a dimension-wise strategy for two main objectives. First, to derive more robust holistic embeddings with improved generalizability [1, 14, 15, 20, 51, 57, 59], and second, to explicitly decompose images into latent factors, each corresponding to distinct and semantically meaningful attributes, in order to improve explainability [4, 12, 62, 65].

In medical imaging, the motivations for DRL are especially strong: improved interpretability, controllability, and robustness to confounding factors are crucial in clinical settings [39, 56]. When transitioning DRL to medical imaging, researchers seek to decouple anatomical properties (*e.g.*, or-

gan size or shape) [31, 58], modality characteristics (*e.g.*, CT and MRI sequences) [8, 46], and pathological factors (*e.g.*, tumor presence or severity) [29, 38], aiming to isolate distinct clinical features.

Despite notable progress, data- and perturbation-driven DRL approaches can be sensitive to training objectives, architecture choices, and assumptions about independent factors [40, 57, 59]. In existing studies, disentangled dimensions may not align precisely with real anatomical or pathological concepts, and spatial correspondence often remains weak when images are globally encoded. Consequently, there has been a growing emphasis on methods that combine disentanglement principles with controlled grouping or tokenization schemes to encapsulate semantically meaningful subsets of features.

### **B.** Implementation Details

### **B.1. Image Preprocessing**

For all 3D medical volumes, we standardize the spatial resolution to  $2.0 \, \text{mm} \times 2.0 \, \text{mm} \times 2.0 \, \text{mm}$  and apply a center crop of  $224 \times 224$ . For CT datasets, we clip intensity values to the [-1000, 1000] Hounsfield Unit (HU) range and normalize them to [0,1]. For MRI datasets, we clip intensities to the [0,99] percentile range and normalize them to [0,1]. We define five token groups to extract semantic features based on common annotations: background, liver, kidneys, spleen, and pancreas. Each medical image is further standardized in thickness by center-padding or cropping 112 slices based on the anatomical centers of the four organs.

For the Abdomen1K dataset [42], the number of cases in the training and test sets is 899:101. For AutoPet [21], the split is 700:200, while for RAOS delay and pre-artery sequences [41], both have a training-to-test ratio of 330:83. All experiments, including OWT, MAE, and segmentation networks, are based on the same preprocessed dataset.

For the 2D face images in CelebAMaskHQ dataset [36], we resize them to  $224 \times 224$ , and define six semantic entities based on annotations (background, face&ear, hair&hat, mouth, nose, and eyes&glasses), as shown in Fig. 8. The CelebAMaskHQ dataset contains 30,000 facial image cases, with 24,000 images allocated for training and 6,000 for testing.

### **B.2. Default Architecture of OWT and MAE**

In OWT, we adopt the same encoder and decoder architecture as MAE [28], with the only modification being the re-

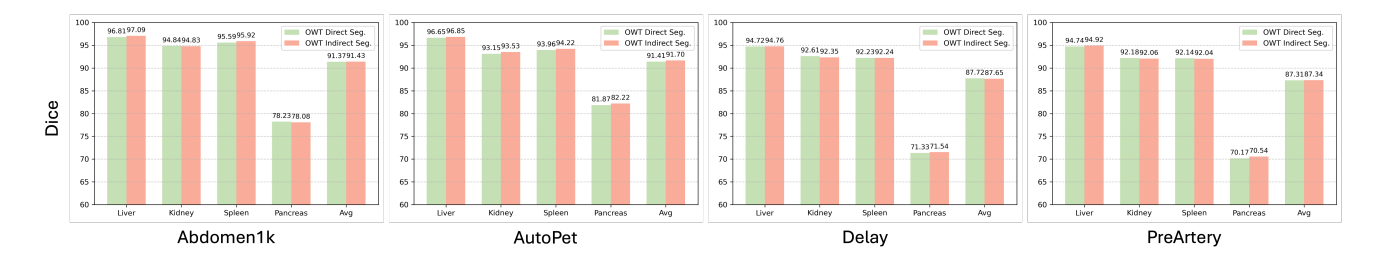


Figure 10. Comparison of segmentation performance using direct and indirect approaches.

Method	Auto	oPet	CelebAMaskHQ		
	L2 ↓	LPIPS ↓	L2 ↓	LPIPS ↓	
MAE/LPIPS	2.77e-04	0.0255	2.78e-03	0.1157	
OWT	1.49e-04	0.0232	2.50e-03	0.1101	
$OWT/_{VQGAN}$	6.89e-05	0.0073	1.80e-03	0.0540	

Table 11. Performance comparison when altering the Transformer-based encoder and decoder to those of VOGAN.

placement of the self-attention blocks [54] with linear self-attention blocks [32]. The hyperparameters, optimizer and scheduler settings all follow MAE. By default, we use the ViT-base architecture, where the MAE encoder consists of 12 attention blocks, the decoder has 8, and the token embedding dimension is set to 768. For OWT, we configure the Encoder and Token Group Encoder with 6 attention blocks each, while keeping the decoder at 8 blocks. This ensures that the overall model length remains consistent with MAE.

The default token number for each token group is 20 in OWT. Therefore, the training load of OWT is lower than that of MAE when using fewer than 10 SDTGs. To prevent information leakage during TGR training, we remove the class token from the OWT architecture. For OWT processing 2D images, we use a  $16\times16$  kernel for patch embedding. For 3D input volumes, we apply a  $1\times16\times16$  3D kernel for patch embedding.

### **B.3.** Experimental Setup

We follow the same experimental setup and hyperparameter settings as MAE. Additionally, each MAE- and OWT-based experiment is trained for 1200 epochs, with a 60-epoch warm-up phase. The training follows the learning rate protocol lr = base\_lr  $\times$  effective\_batch\_size/256 where the base learning rate is set to base\_lr =  $10^{-4}$ .

For OWT with 2D image inputs, we set the batch size to 96. When processing 4-slice medical volumes, the batch size is set to 64. In medical imaging training, each unique input (whether a single slice or a 4-slice volume) is treated as an individual input. For instance, a 3D medical volume with a thickness of 112 slices is considered as 112 separate inputs during training. An epoch is defined as the point

when all unique inputs in the dataset have been processed once.

For MAE training, we randomly mask 75% of the tokens. During testing, we adjust the mask ratio to 0.25 for improved performance. When MAE is trained with LPIPS loss, all tokens are preserved for image reconstruction.

All reconstructed images are filtered with a 0.02 pixelrange threshold to reduce background noise. For the interpretability experiments validated by segmentation, we apply a 0.15 threshold to transfer the reconstructed results as semantic masks.

# C. Detailed Settings of Multi-Modality Incorporation

For the OWT experiment incorporating text encoding, we design a text prompt inspired by [37]. Specifically, we define the template as "a computerized tomography [category]", where [category] corresponds to "background without the Liver, Kidneys, Spleen, and Pancreas", "of a Liver". "of Kidneys", "of a Spleen", and Pancreas", aligning with the number of token groups. These 5 prompts are fed into a CT-specific pretrained CLIP text encoder, CT-CLIP [25] to obtain the corresponding CT-consistent text encoding, resulting in a representation of size  $5 \times 512 \times 768$ . Then, the mean is taken along the middle dimension, yielding a representation of size  $5 \times 768$ .

To match the dimension token groups, we replicate each text encoding according to the number of tokens per token group (20), leading to a final text encoding dimension of  $100 \times 768$ . Within the OWT framework, a linear transformation layer maps the text encoding from 768 to 768, resulting in a transformed text embedding of the same size  $100 \times 768$ . This transformed text encoding is then element-wise added to the organ-wise representation  $X_G$  extracted by the Organ Collector. The combined representation proceeds through the random selection procedure in TGR, while all other components remain consistent with the default OWT settings.

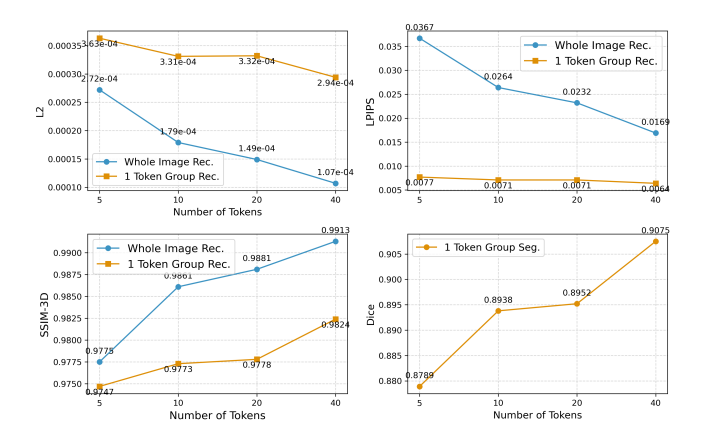


Figure 11. Ablation study on the number of tokens in each token group when trained on AutoPet.

AutoPet	Holisti	Holistic Rec.		1 Token Group Rec.	
OWT	L2 ↓	LPIPS ↓	L2 ↓	LPIPS ↓	
_	1.49e-04 1.40e-04		3.32e-04 <b>3.19e-04</b>	0.0071 <b>0.0067</b>	

Table 12. Reconstruction comparison of OWT with regular and adaptively distributed SDTGs.

### **D. Ablation Studies**

For the ablation study, we explore the following key aspects: the flexibility of the encoder-decoder architecture, the number of tokens per SDTG, and the impact of varying the amount of input data and labels in OWT.

#### **D.1. Backbone Alteration**

We investigate the effect of replacing the default ViT-based encoder-decoder architecture in OWT (adopted from MAE) with the encoder and decoder from VQGAN [17]. Specifically, we configure the VQGAN bottleneck dimensions to  $14 \times 14$  for a  $224 \times 224$  input image, ensuring that the number of latent tokens (196) remains consistent with the ViT-based setting. As shown in Table 11, despite the increased computational cost of VQGAN's hybrid CNN and self-attention structure, it achieves significant performance gains over the transformer-based encoder-decoder. On two datasets, it improves both L2 and LPIPS evaluation metrics by 53.8%–68.5% in AutoPet and 43.8%–51.0% in CelebA-MaskHQ, demonstrating the potential for further enhancements in OWT and highlighting its architectural flexibility.

### D.2. Number of Tokens per SDTG

The number of tokens within each SDTG determines its capacity to store organ-specific information. To evaluate this, we experiment with SDTG token counts of 5, 10, 20, and 40, assessing their impact on both generation and segmen-

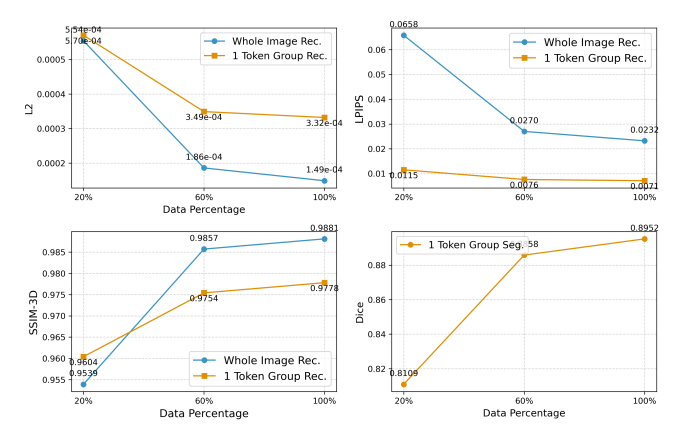


Figure 12. Ablation study on OWT performance when utilizing different percentages of the dataset (AutoPet).

tation tasks. For the generation task, we measure full-image reconstruction using all SDTGs and single-organ reconstruction using only one SDTG, evaluated by L2, LPIPS, and SSIM-3D metrics. For segmentation, we assess the Dice score of single-organ masks.

As shown in Fig. 11, increasing the token count from 10 to 20 provides a slight performance improvement, while further increasing it from 20 to 40 leads to a more significant boost. This suggests that OWT has considerable scalability and potential as a foundational semantic-level tokenization framework, capable of further enhancements with increased token capacity.

### D.3. Adaptively Distributed SDTGs

To explore this, we include a proof-of-concept experiment showing that the OWT framework has the potential to support adaptive token group sizing. We allocated token numbers to different organs based on the fourth root of their volumes. For background (containing all information other than defined organs), liver, kidney, spleen, and pancreas, 45, 20, 13, 13, and 9 were allocated, with the total tokens fixed at 100 (identical to the default setting). Preliminary results show that this adaptive allocation better accommodates the varying feature distributions across organs and provides performance improvements over a fixed-size setting (Table 12), demonstrating the scalability of OWT as a novel foundational tokenization framework.

### **D.4. Data Percentage**

Fig. 12 illustrates the performance of the OWT framework on the AutoPet dataset when trained with 20%, 60%, and 100% of the data. We observe a significant improvement in performance when increasing the dataset size from 20% to 60%, whereas the gain from 60% to 100% is relatively marginal. This suggests that OWT efficiently learns meaningful representations with a moderate amount of data, in-

Abdomen1k	Liver	Kidney	Spleen	Pancreas	Avg Dice ↑
UNetplus	96.85	94.63	91.00	71.05	88.38
AttU_Net	97.09	95.22	93.05	72.00	89.34
TransUnet	96.78	94.65	92.30	71.89	88.91
SwinUnet	96.53	93.68	90.52	65.50	86.56
CMUNet	96.05	94.67	90.84	71.75	88.33
OWT	96.55	94.21	95.12	71.32	89.30
OWT/ <sub>4-slice</sub>	96.81	94.84	95.59	78.23	<b>91.37</b> <sub>+2.03</sub>
AutoPet	Liver	Kidney	Spleen	Pancreas	Avg Dice ↑
AutoPet UNetplus	Liver 96.41	Kidney 92.56	Spleen 91.31	Pancreas 76.87	
					Avg Dice ↑
UNetplus	96.41	92.56	91.31	76.87	Avg Dice ↑ 89.29
UNetplus AttU_Net	96.41 96.60	92.56 92.86	91.31 91.22	76.87 78.24	Avg Dice ↑  89.29  89.73
UNetplus AttU_Net TransUnet	96.41 96.60 96.34	92.56 92.86 <b>93.59</b>	91.31 91.22 90.65	76.87 78.24 78.23	Avg Dice ↑  89.29  89.73  89.70
UNetplus AttU_Net TransUnet SwinUnet	96.41 96.60 96.34 96.33	92.56 92.86 <b>93.59</b> 92.34	91.31 91.22 90.65 91.11	76.87 78.24 78.23 72.46	Avg Dice ↑  89.29  89.73  89.70  88.06

Table 13. Performance of semantic segmentation on CT datasets.

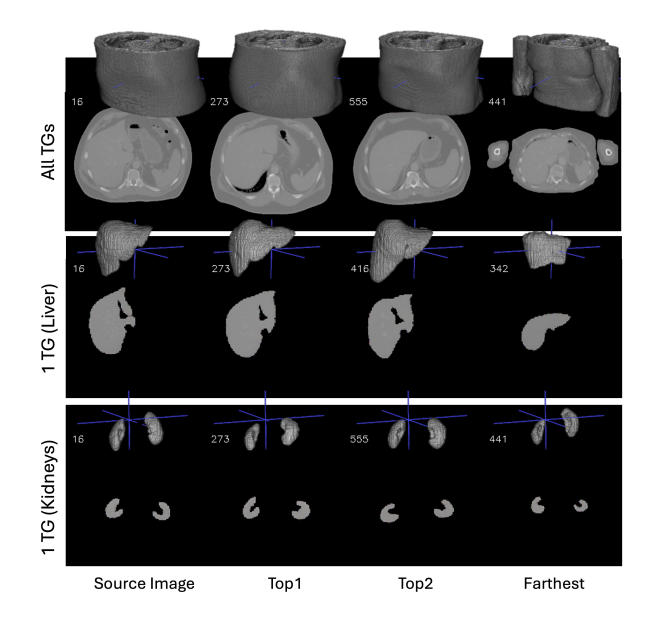


Figure 13. Semantic-based retrieval of CT images.

dicating its strong data efficiency and the potential for effective generalization even with limited training samples.

### **E. Detailed Semantic Segmentation Results**

**Detailed Results.** Tables 13 and 14 provide a more detailed results of those presented in Table 6, showing the Dice scores for each of the four organs across different datasets. From Tables 13 and 14, we observe that compared to dedicated segmentation networks, OWT/4-slice generally achieves superior performance across all organs. No-

Delay	Liver	Kidney	Spleen	Pancreas	Avg Dice ↑
UNetplus	93.53	91.85	85.20	65.85	84.11
AttU_Net	94.25	91.08	86.85	65.98	84.54
TransUnet	93.93	90.83	89.07	66.03	84.97
SwinUnet	92.78	90.61	86.35	62.55	83.07
CMUNet	94.02	91.88	87.74	65.64	84.82
OWT	94.32	91.87	91.55	65.65	85.85
OWT/ <sub>4-slice</sub>	94.72	92.61	92.23	71.33	$87.72_{+1.87}$
PreArtery	Liver	Kidney	Spleen	Pancreas	Avg Dice ↑
PreArtery UNetplus	Liver 94.05	Kidney 92.25	Spleen 87.26	Pancreas 64.14	Avg Dice ↑
UNetplus	94.05	92.25	87.26	64.14	84.42
UNetplus AttU_Net	94.05 94.33	92.25 92.32	87.26 89.07	64.14 64.45	84.42 85.04
UNetplus AttU_Net TransUnet	94.05 94.33 94.33	92.25 92.32 90.69	87.26 89.07 86.59	64.14 64.45 65.56	84.42 85.04 84.29
UNetplus AttU_Net TransUnet SwinUnet	94.05 94.33 94.33 92.91	92.25 92.32 90.69 88.91	87.26 89.07 86.59 86.33	64.14 64.45 65.56 61.48	84.42 85.04 84.29 82.41

Table 14. Performance of semantic segmentation on MRI datasets.

tably, for smaller organs such as the pancreas,  $OWT/_{4\text{-slice}}$  demonstrates a significant improvement, with an advantage exceeding a 5.3 dice score in the best case.

Token Group Connectivity. For semantic segmentation using OWT, we generate masks by processing independently utilized Semantically Disentangled Token Groups (SDTGs) through the Token Group Encoder, AHER, and decoder to reconstruct an image, which is then thresholded to produce a segmentation mask. We refer to this mask as the "direct" mask. Since SDTGs can be flexibly combined, we also explore an alternative approach: subtracting the reconstructed images from all other four SDTGs from the input image and applying a threshold to obtain a predicted mask for the same organ. We define this as the "indirect" mask.

Although using all complementary SDTGs reduces computational efficiency compared to single SDTG usage, it incorporates additional inter- and intra-organ information, potentially enhancing connectivity in the segmentation process. To evaluate whether leveraging more SDTGs improves boundary and shape reconstruction, we conduct comparative experiments. The results, presented in Fig. 10, show that across four datasets, the direct and indirect methods yield largely similar outcomes. This demonstrates that the SDTGs extracted by OWT maintain a high degree of semantic independence, as they accurately capture organ boundaries and shapes even when used independently. These findings align with the t-SNE visualization of SDTG relationships in Fig. 6, further validating their disentangled nature.

# F. Additional Organ-Level Retrieval Demonstration

An additional example demonstrates OWT performing organ-level retrieval on the CT modality (Fig. 13). Combined with Fig. 5, this shows the stability and potential of OWT for organ-level retrieval across different modalities. It can not only retrieve patients with similar body shapes at a holistic level, but also retrieve organs in similar conditions and locations for specific organs of interest. This highlights the more flexible and unique clinical value of OWT, which cannot be achieved by existing retrieval methods based on holistic embeddings.